![AGU 100 ADVANCING EARTH AND SPACE SCIENCE logo]

Geophysical Research Letters

RESEARCH LETTER
10.1029/2018GL079343

Yield Estimate (230 kt) for a Mueller-Murphy Model of the 3 September 2017, North Korean Nuclear Test (m_{bNEIC} = 6.3) From Teleseismic Broadband *P* Waves Assuming Extensive Near-Source Damage

Esteban J. Chaves[1,2] (iD), Thorne Lay[1] (iD), and Dimitri P. Voytan[1]

[1]Department of Earth and Planetary Sciences, University of California, Santa Cruz, CA, USA, [2]Volcanological and Seismological Observatory of Costa Rica, Universidad Nacional (OVSICORI-UNA), Heredia, Costa Rica

Abstract The 3 September 2017 underground nuclear test (m_{bNEIC} = 6.3) is the largest of six announced North Korean explosions. The event generated many *P* wave seismograms at global broadband seismic stations with good signal-to-noise ratio for periods less than ~5 s. Instrument deconvolution provides 435 stable broadband *P* wave ground displacement records in the period range 0.1 to 5.0 s. These are stacked in 26 azimuth/distance windows to average path and receiver effects. Waveform stacks and average amplitude of 4-Hz ground displacements are modeled assuming a Mueller-Murphy explosion source model for a granite source medium. Nonelastic *pP* delays consistent with burial depths in the mountainous source topography are considered, and explosion yield and an average constant-*Q* attenuation operator are estimated by fitting the waveforms. For a source depth of 750 m in heavily damaged environment, the estimated yield = 230 ± 50 kt and *t** = 0.78 ± 0.03 s.

Plain Language Summary Seismic *P* wave ground motions recorded around the world for the 3 September 2017 underground nuclear test at the North Korean test site are modeled to constrain the explosion yield and the average path attenuation parameter. Broadband ground motion waveforms are modeled along with the amplitude of 4-Hz ground motions, exploring a wide range of attenuation and yield parameters along with allowing for nonelastic behavior of the *P* wave reflection (*pP*) from the free surface above the explosion, which travels down through the damage zone surrounding the explosion-produced cavity. For a source depth of 750 m, which is reasonable for location of the explosion under the mountain peak, and allowing for an extensive damage zone, the waveform modeling provides an estimated yield of 230 ± 50 kt. Yield estimates of smaller events are made based on calibration of magnitude-yield relations using this result and range from 0.5 to 17.8 kt.

1. Introduction

On 3 September 2017, the Democratic People's Republic of Korea (DPRK) conducted its sixth and largest declared underground nuclear test at the Punggye-ri nuclear test site (03:30:01.760 UTC, 41.332°N, 129.030°E; U.S. Geological Survey/National Earthquake Information Center [USGS/NEIC], https://earthquake.usgs.gov/earthquakes/eventpage/us2000aert#executive). The ~1-s period body wave magnitude, m_{bNEIC} 6.3, reported by USGS/NEIC was obtained from 941 stations. This is one magnitude unit larger than for the largest previous test on 9 September 2016 (m_{bNEIC} 5.3). Estimates of explosion yield (*W*) based on various magnitude-yield relationships ($m_b = a + b \log W$, where *a* and *b* are constants) calibrated for other test sites span a wide range for the DPRK tests (e.g., Murphy et al., 2013), due to uncertainty in site-specific coupling effects, likely overburial of the tunnel-emplaced events, and poorly constrained crustal and mantle attenuation for the test site. Lacking a direct calibration shot of known size, modeling the recorded ground motions is the most promising approach to narrowing yield uncertainty of the DPRK tests (e.g., Wang et al., 2018).

The 2017 explosion produced good signal-to-noise ratio broadband teleseismic *P* wave recordings at hundreds of global stations (Figure 1), along with high-quality regional recordings. Regional waveforms have complicated propagation effects that are sensitive to unknown details of the 3-D structure, while teleseismic *P* waveforms have relatively simple propagation effects but poorly constrained anelastic effects and possible
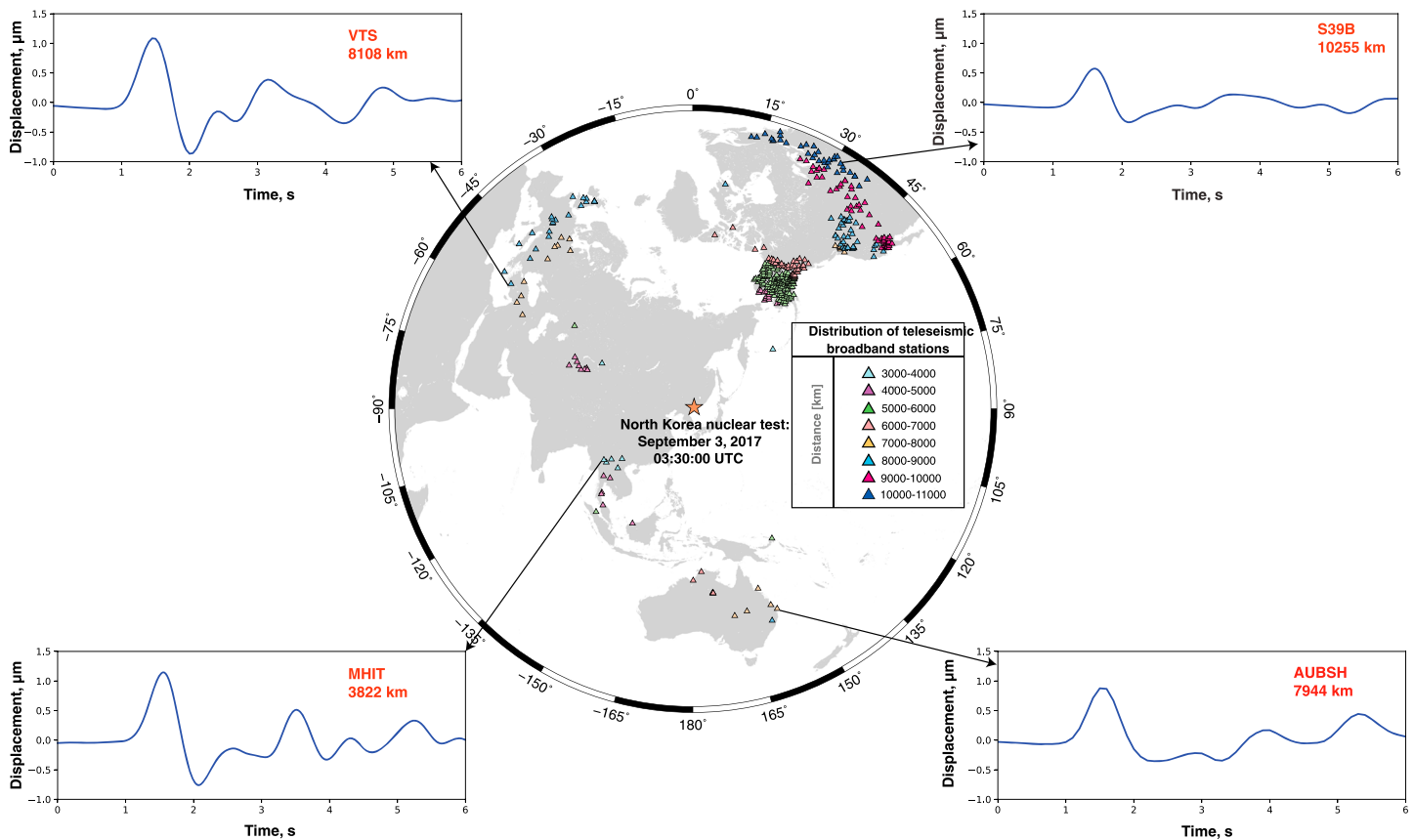
Figure 1. Spatial distribution of teleseismic *P* wave recordings by broadband seismic stations (triangles) used in this study. The red star denotes the epicenter of the 3 September 2017, North Korean nuclear test (m_{bNEIC} = 6.3). Stations are color coded by distance bins. The vertical component *P* waves from the 435 stations are stacked in distance and azimuth bins (Figure S1). Representative broadband ground displacement waveforms from individual stations are shown for each quadrant.

complexity of free-surface reflections (*pP*) from surface topography and transit downward through the explosion damage zone. When broadband instrument responses are removed from the recordings and long-period noise is suppressed, teleseismic *P* wave ground displacement signals for the 2017 explosion have simple waveforms (Figure 1), amenable to modeling.

Efforts to model teleseismic broadband *P* wave ground motions for large nuclear explosions commenced with Burdick and Helmberger (1979), who jointly deconvolved short-period and long-period WWSSN recordings to estimate the ground displacements, a rather unstable procedure. They demonstrated that the broadband waveforms provide sensitivity to arrival time and amplitude of the free-surface reflection, *pP*, as well as to overshoot of the explosion reduced displacement potential. Subsequent single station and multichannel deconvolutions of digital short-period recordings from seismic arrays also provided estimates of broadband *P* wave ground displacements with apparently delayed *pP* arrivals (e.g., Der et al., 1987; Douglas et al., 1987). For modern broadband digital recordings, it is straightforward to recover stable broadband *P* wave ground displacements, and the 2017 event provides by far the most extensive data set of this type for any nuclear test. We model this unique data set to constrain the source properties.

2. Data and Modeling Procedure

Over 2,500 teleseismic vertical component broadband and short-period *P* wave recordings from stations assembled by the Incorporated Research Institutions for Seismology are deconvolved by their instrument responses to produce broadband ground displacements in the passband 0.1 to 5 s. Deconvolved *P* wave displacements were also filtered with a causal high-pass (>4-Hz) filter. Screening for signal fidelity, 435 broadband signals with stable baselines and impulsive *P* wave onsets (Figure 1) and 517 4-Hz displacements are retained (Figure 2).
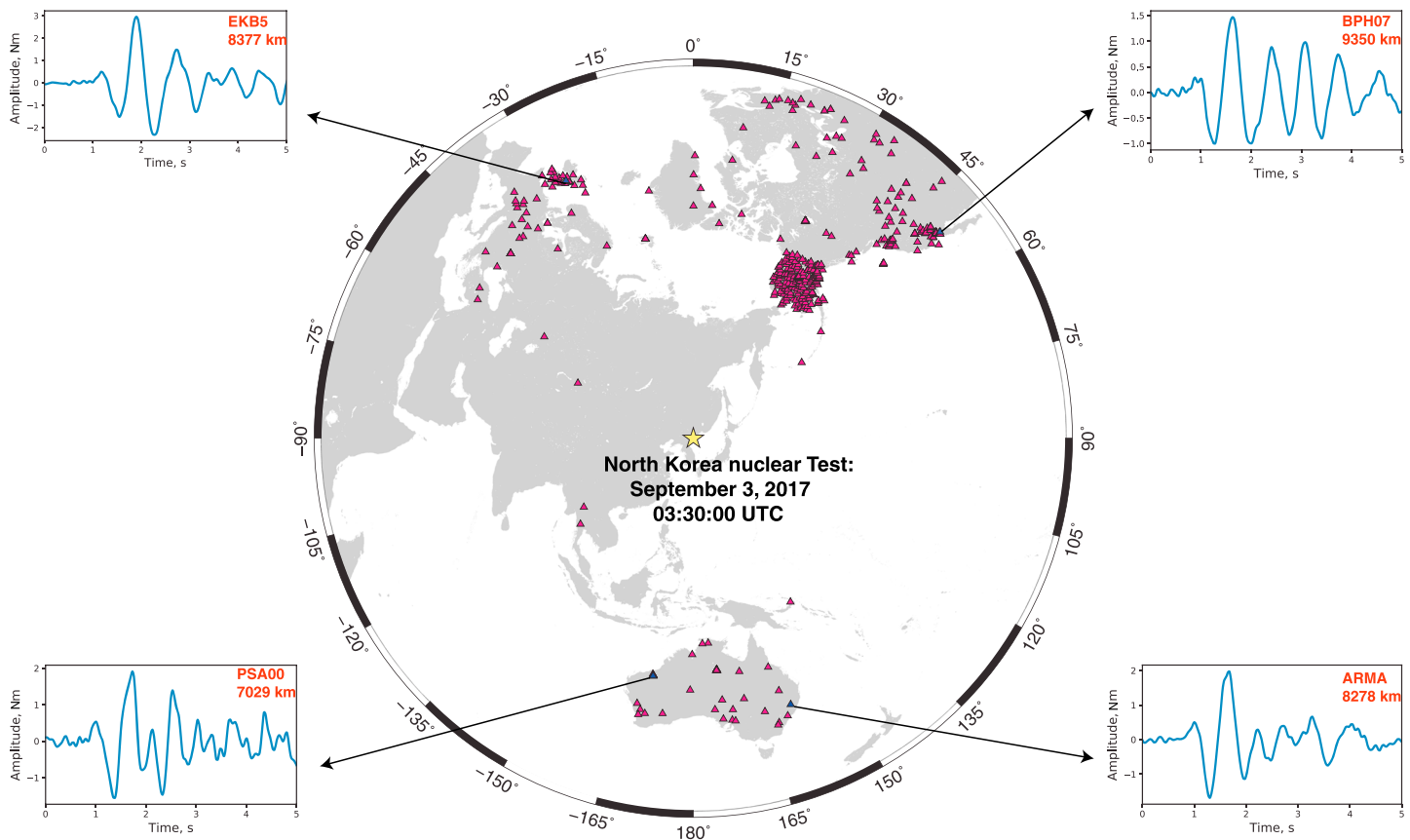
Figure 2. Spatial distribution of teleseismic *P* wave ground motions filtered above 4 Hz used in this study. The red star denotes the epicenter of the 2017 nuclear test. The first-peak to first-trough amplitude of high-pass filtered vertical component *P* waves from 517 stations (Figure S2) are corrected for geometric spreading to 5,500 km and logarithmically averaged, giving a value of 2.68 nm. Representative 4-Hz ground displacement waveforms from individual stations are shown.

Each broadband signal has an initial ~1-s duration half-cycle of ground motion followed by path/station-specific complexity of the *P* coda. These signals are binned in 20° azimuth and 1,000-km distance windows (supporting information Figure S1). We align individual waveforms on the first-motions and apply geometric spreading corrections to the bin midpoints before computing a linear stack for each bin. This suppresses individual station variations and focusing and defocusing by variable 3-D earth structure, while enhancing common source contributions for the average azimuth and ray-parameter corresponding to each bin location. These stacks provide balanced ground displacement time series used in the modeling. The peak amplitude of a spreading-corrected (to 5,500 km) stack of all 26 broadband bins is 1.151 μm.

The average first-peak to first-trough amplitude of the spreading-corrected (to 5,500 km) 4-Hz filtered displacements (Figure S2) is 2.68 nm (1.34- to 5.33-nm range for standard deviation from logarithmic mean), a value we also model. Each 4-Hz filtered waveform has an onset-time-to-first-trough interval of ~0.25 s, which is on the order of the expected elastic *pP* time, so these provide *P* wave measurements that are almost insensitive to *pP* (Figure S3).

When modeling teleseismic recordings, *P* wave attenuation must be accounted for. Attenuation is strongest in the upper mantle and varies laterally, so each path has some specific attenuation, which may be frequency dependent. But detailed information about the attenuation for each path is unknown; in particular, there is no strong constraint on the attenuation in the crust and upper mantle beneath the DPRK test site, which affects all teleseismic paths. Source region attenuation influences both the intercept and slope parameters of the magnitude-yield scaling relationship for the test site. Observed broadband *P* wave displacements for the 2017 event have very similar shape in the first second of ground motion at all azimuths and distances (Figures 1 and S1); thus, we empirically determine a best choice of average parameterized attenuation operator for the full set of observations. We consider both frequency-independent attenuation, constant *t** operators

(Futterman, 1962), and frequency-dependent absorption band attenuation, $t^*(f)$ operators (Minster, 1978). There are strong variations in attenuation beneath each station, and we rely on averaging of many paths with unknown individual attenuation parameters to achieve stable results. Similar extensive averaging goes into computing magnitudes used in a magnitude-yield relationship, but magnitudes are not explicitly corrected for source function scaling, coupling, or depth of burial so they require empirical calibration.

We assume a broadband representation of the explosion source time function, for which various models have been proposed (e.g., Denny & Johnson, 1991; Haskell, 1967; Helmberger & Hadley, 1981; Mueller & Murphy, 1971; von Seggern & Blandford, 1972). We adopt the Mueller-Murphy (MM) source model, as it is the most fully calibrated model, with extensive application (e.g., Saikia, 2017; Stevens & Day, 1985; Walter & Priestley, 1991). This source model is explicitly prescribed for a given yield (W) and depth of burial (H) in a particular source medium. We assume standard parameters for a granite medium (Stevens & Day, 1985), which is considered appropriate for the North Korean source region (Murphy et al., 2013; Saikia, 2017); this is directly related to the coupling issue and influences the magnitude-yield intercept level (a, the 1 kt m_b value). Saikia (2017) recently presented an analytic formulation of the time-domain far-field reduced velocity potential (RVP) that is convenient for broadband waveform modeling. There are uncertainties in the scaling behavior for the MM model (e.g., Patton & Pabian, 2014), as is true for all source models. Our results are coupled to that particular model.

Finally, we must prescribe the propagation structure and method of computing the impulse response Green's functions. We consider both half-space far-field first-motion approximation and plane-layered source and receiver structure reflectivity responses for constant ray parameters for each data bin. Geometric spreading is computed for a 1-D Jeffreys-Bullen radial velocity model with either a surface velocity of 5.5 km/s or a mantle velocity of 8.0 km/s at the base of the source and receiver reflectivity structures (Table S1). Studies of teleseismic P waves from prior large nuclear tests at U.S. and Soviet test sites indicate that pP can be delayed by factors of 1.5–2.0 relative to elastic predictions and in some cases reduced in amplitude relative to elastic predictions (e.g., Lay, 1991), due to a combination of strong spall and surface cratering effects and damage of the elastic medium around the shot point. The 2017 event did not produce spall, but significant mountain deformation is indicated by InSAR (Wang et al., 2018). We parameterize perturbations of the elastic delay time and amplitude of pP with multiplicative factors pPtime (the elastic pP-P time is multiplied by this factor) and pPamp (the pP reflection coefficient is multiplied by this factor), respectively, to account for nonelastic effects on pP.

The North Korean test site involves tunnel-emplaced shots within a mountain with up to 800 m overburden relative to the tunnel adit. Numerical calculations demonstrate that the topography produces azimuthal patterns of pP arrivals and surface scattering relative to predictions for a flat free surface, but this depends on precise placement of the explosion within the topography (e.g., Avants, 2014). With data averaging and the simplicity of teleseismic waveforms modeled here, the degree to which the flat structure responses may be biased appears secondary, and the dominant effects of attenuation and nonelastic pP preclude observational assessment of this issue.

We construct synthetics for each of the 26 binned broadband P waveforms, using weighted average normalized cross-correlation coefficients and weighted average least-squares waveform differences for the first second of each waveform to evaluate the overall fit to the data. Weighting is based on relative number of waveforms in each stack. We forward model the data using a grid search over W (70–560 kt), H (650–800 m), and t^* (0.3–1.1 s), with pPtime values from 1.0 to 3.0 (pPamp deviations from elasticity were found to have secondary influence and are not discussed here). Modeling with $t^*(f)$ favored negligible frequency dependence, so only results with constant t^* are presented here. Undoubtedly, some paths do have frequency-dependent attenuation parameters (e.g., Der et al., 1982), but the waveforms for our elastic models strongly favor an average constant Q model with frequency independent t^*. Use of one of the other source model parameterizations with a different spectral decay rate could favor a $t^*(f)$ model (e.g., Burger et al., 1987).

3. Results

The high velocity of the hard-rock source medium produces pP delay times of ~0.25 s for considered burial depths, and elastic free surface reflection coefficients of ~ −0.8; this produces destructive interference between the P and pP arrivals in the broadband data but slight constructive interference in the 4-Hz data. The explosion RVP first half-cycle duration is about the same as the pP delay time for the MM models, so
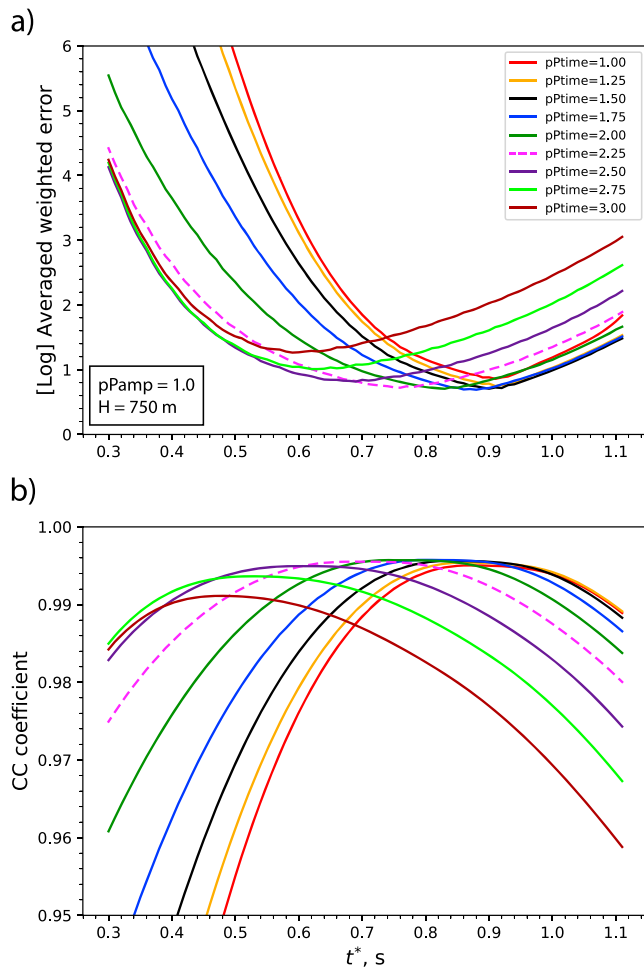
a)

b)

Figure 3. (a) Logarithmic average weighted error between observed and synthetic broadband *P* waves for varying combinations of t^*, *pP*time factor and yield (optimal yield is used for minimizing each point on each curve), for *H* = 750 m and *pP*amp = 1.0 (elastic). (b) Corresponding average weighted correlation coefficients.

the far-field source-function has a two-sided shape, with an ~0.25-s duration upswing followed by a weaker downswing. Convolution with the t^* operator broadens the signal to a first half cycle duration of ~1 s in order to match the data, thus the far-field waveforms do not directly display the *pP* interference in the time domain, even though the effect is present (Figures S4 and S5). Computation of event-averaged amplitude spectra (e.g., Murphy et al., 2013) also does not provide direct resolution of the *pP* properties because the main *pP* effect is at high frequencies that are hard to recover due to attenuation uncertainty.

For initial elastic *pP* calculations, we found that for both half-space and layered source and receiver structures there is little sensitivity to burial depth over the range 700 to 800 m, for t^*-*W* combinations that match the broadband data well. Waveform matches degrade for shallower burial depths (Figure S6). Almost all precise locations and relative locations place the 2017 epicenter beneath the maximum (800 m) overburden near the peak of Mt. Mantap relative to the tunnel adit, so we show results here for *H* = 750 m. This determines the shotpoint pressure, utilized in the MM model, and is consistent with mildly shallowing tunneling practices for most tunnel shots (Wang et al., 2018 estimate a source depth of 450 m, which is very shallow from the containment perspective). As the explosion yield is certainly larger than 100 kt, a substantial cavity and damage zone is expected, and *pP* is expected to be delayed by downward transit through the damage zone.

Figure 3 displays, for *H* = 750 m, how the waveform mismatch error varies as a function of t^* for varying nonelastic *pP* delays (*pP*time = 1.0 and *pP*amp = 1.0 give the elastic calculation). For each t^*, the yield is chosen that best matches the data, so yield varies along these curves. When *pP*time exceeds 2.25 both waveform error and average cross-correlation degrade, but up to that value there is a systematic reduction of the average t^* estimate. This is because *pP* delay causes decreasing destructive interference in the broadband pulse, so a lower t^* is needed to match the amplitudes. For values of *pP*time from 1.5 to 2.25 the fits are better than the elastic case, favoring t^* values of 0.75 to 0.88 s, but the differences are modest.

Figure 4 displays the variation of broadband waveform error and cross-correlation measures for two cases with *H* = 750 m; (a) and (b) show the results for elastic models, and (c) and (d) show the results for nonelastic *pP*time = 2.25, which produces *pP* lag times of up to 0.56 s, corresponding to an extensive damage zone. The contours for the average correlation fits exceeding 0.995 from the right panels are superimposed on the left panels to highlight intersecting areas of low waveform misfit and high waveform correlation. Also superimposed on the left panels are white curves indicating the t^*-*W* combinations that match the average 4-Hz amplitude of 2.68 nm for the corresponding models. These curves have much less sensitivity to the *pP* parameters (Figure S3) and greatly narrow the range of models that can be deemed acceptable for the 2017 source.

For the elastic *pP* parameters (Figures 4a and 4b), a viable match to combined broadband and high-frequency data is provided obtained using *W* = 456 kt and t^* = 0.88 s. Given the likelihood of a substantial damage zone impact on *pP* timing, a model with *W* = 230 kt, t^* = 0.78 s, and *pP*time = 2.25 is also viable, and produces a slightly lower waveform error and higher correlation coefficient than the elastic case, as expected from Figure 3. We prefer the latter model, as it involves a lower t^*, as suggested by regional estimates (discussed below), and it is consistent with the extensive deformation observed for the test site. Constraining residual errors to less than 1.0, we estimate uncertainties for *W* of ±50 kt and for t^* of ±0.03 s for the case of a delayed *pP* arrival used to account for a heavily damaged source region. t^* values lower than 0.75 s do not fit the amplitudes and correlations well for any choice of *pP*time (Figures 4 and S7).
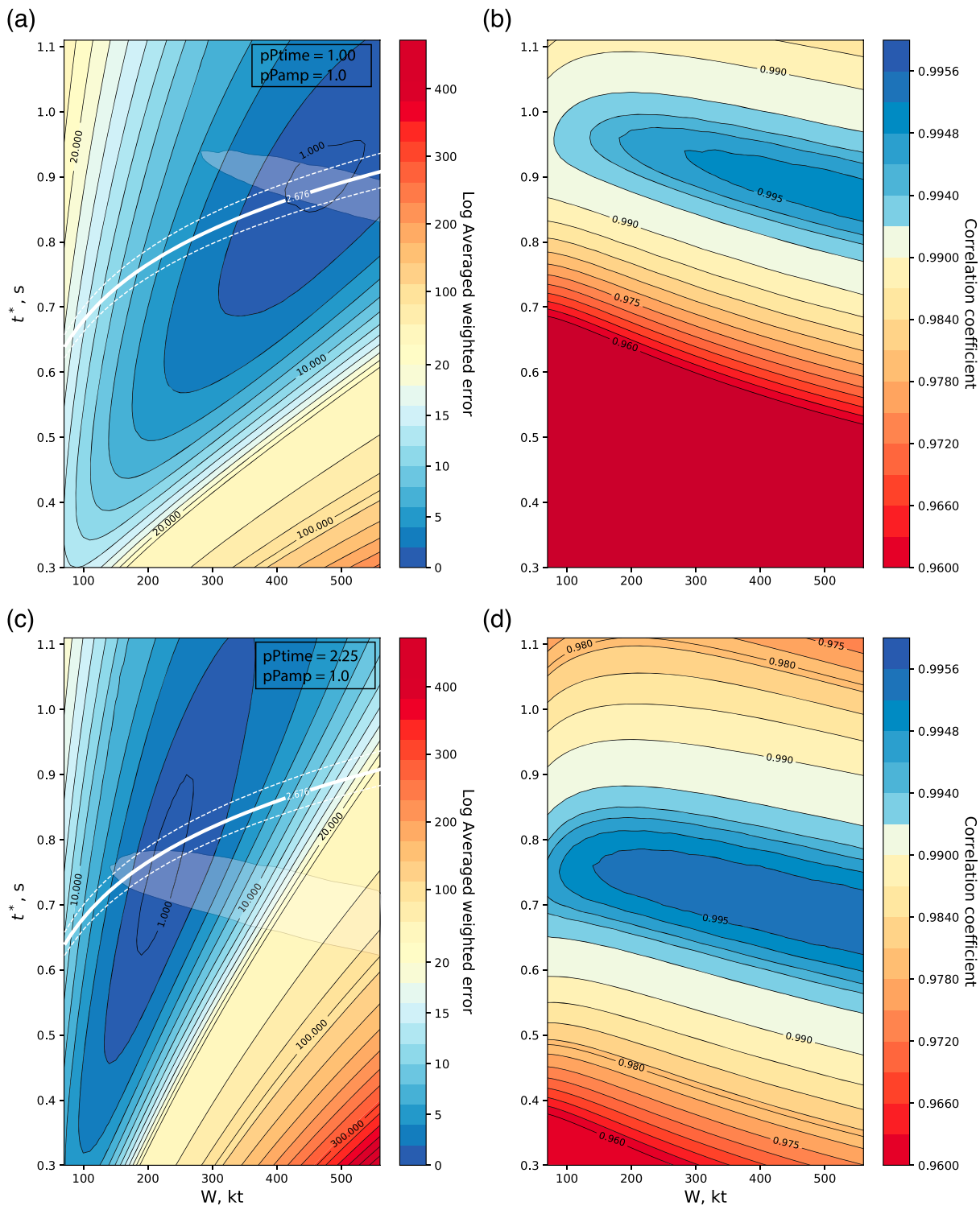
Figure 4. Comparisons of synthetic and observed broadband bin stacks for waveform errors (left) and correlation coefficients (right) for elastic cases (a) and (b), and nonelastic case with pPtime = 2.25 (c) and (d). The contour for cross-correlations of 0.995 from the right panels are superimposed on the left. The white curves indicate the varying t^*-W combinations that match the mean and standard deviation of the observed 4-Hz data amplitudes.

As suggested by the very high normalized-correlation coefficients for the preferred model (~0.995), the wave-form fits are very good for the 1-s duration first displacement pulse, as shown in Figure 5. The predicted wave-forms do not match the extended coda in general, but the waveforms after 1 s are not coherent from stack to
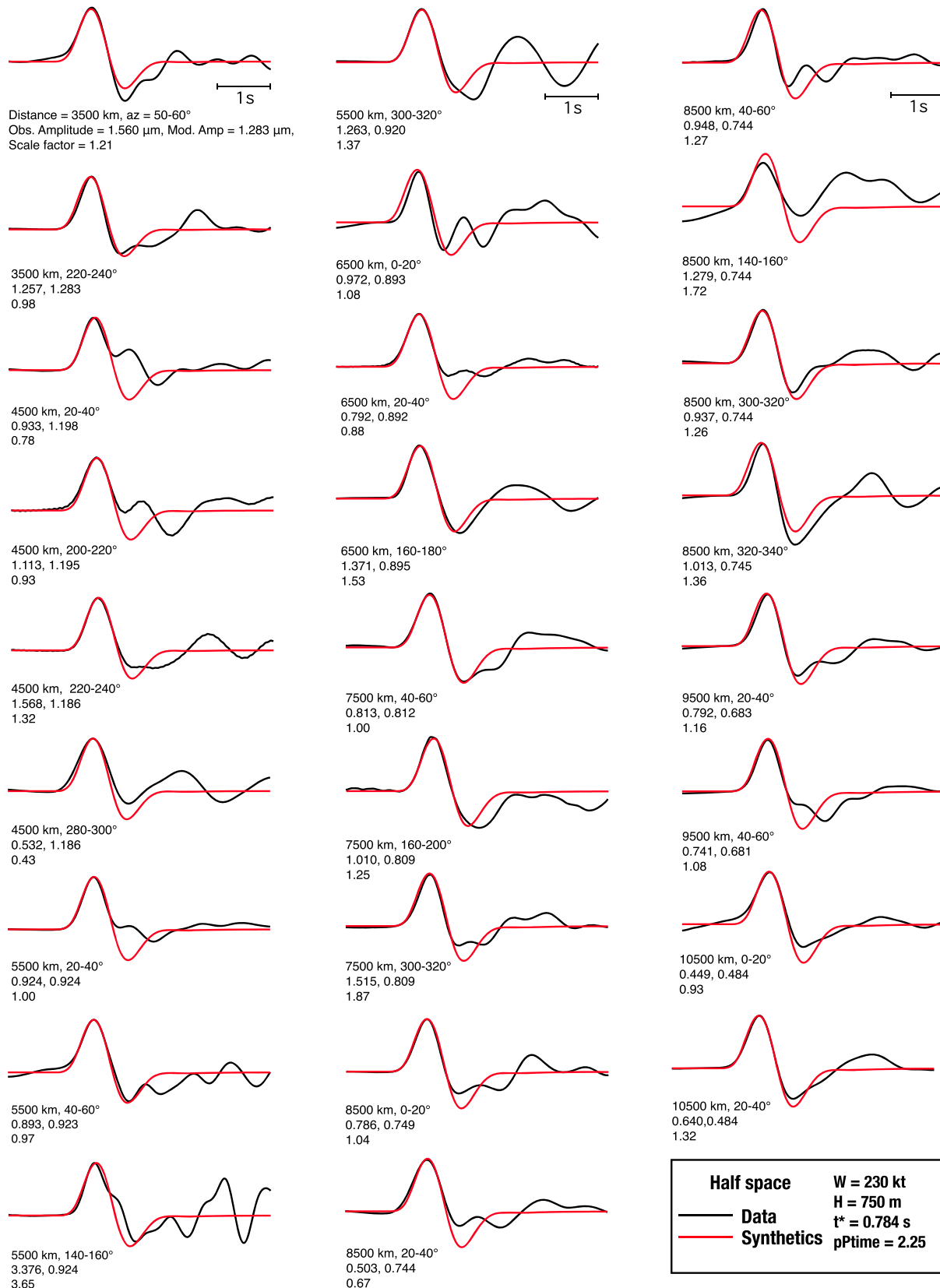
Figure 5. Waveform comparison between stacked observed broadband seismograms in various distance and azimuth bins (black) and synthetics (red) for attenuated ($t^* = 0.78$ s) RVPs ($P + pP$) generated by an explosion source with yield $W = 230$ kt and $H = 750$ m, with a pP delay time factor of 2.25.

stack, indicating that path and receiver effects dominate rather than common or slowly varying source effects. The P and pP waveform interference is completed within the first half cycle of the observed displacement pulses, so the variable coda after 1 s does not provide clear measure of surface interaction or overshoot of the source RVP, although the pPtime = 2.25 case provides better agreement than the elastic case. Amplitude factors that scale the observed and predicted waveforms for each bin show moderate fluctuation; these are a manifestation of differences in receiver functions, path attenuation, spreading, focusing and defocusing, and averaging of station specific effects in each bin. These amplitude variations could also represent azimuthal variations in effective pP amplitudes due to actual near-source topography not accounted for by the flat-lying structure.

4. Discussion and Conclusions

The estimate of an average $t^* \sim 0.78$ s suggests a tectonically active source region, comparable to the Amchitka or Nevada test sites (e.g., Burdick et al., 1984; Burger et al., 1987; Lay et al., 1984), in contrast to the low t^* (≤ 0.50 s) sites at Soviet Semipalatinsk and Novaya Zemlya test sites in stable platform environments (e.g., Bache et al., 1985; Der et al., 1985). Attenuation tomography by Hwang et al. (2011) supports a t^* near the North Korean test site comparable to the high values in the western United States. However, other estimates of regional upper mantle attenuation obtained by Ichinose et al. (2014) and Ni et al. (2010) suggest an average total $t^* \sim 0.5$ s for the DPRK test site. Such a low t^* gives very poor fit to the waveforms (Figures 4 and S6), but our preferred model keeps t^* as low as viable while giving an excellent fit to the data.

The teleseismic data alone do not allow us to resolve all possible trade-offs with pP for nonelastic cases. It is possible that topographic effects on pP and scattered coda from the irregular surface broaden the wavelet emerging from the source region, allowing a lower t^* to match the data, but further numerical modeling for the specific 2017 location and the source surface topography needs to be conducted to evaluate this. Based on the earlier work of Avants (2014) it is not clear that there is any systematic effect.

Assuming this study obtained a correct average path t^* and correctly delayed pP due to heavy damage around the source for the data set analyzed, the 2017 event yield is estimated as 230 ± 50 kt for 750 m burial depth. This explicitly assumes the MM source model is valid; if unresolved model error is considered, the classic 'factor of two' uncertainty (yield from 115 to 460 kt) is a conservative assessment. The preferred model has a computed elastic radius of 923 m and seismic moment = 4.6×10^{16} Nm (M_W 5.11). The scaled-depth of burial factor for this yield and depth is 122 m/W$^{1/3}$, consistent with U.S. testing practice. The yield estimate from Wang et al. (2018) is 120 to 304 kt for a burial depth of 450 m with isotropic component $M_W = 5.05$.

Given one directly determined estimate of yield and the associated m_b from a given network, we can set the baseline in m_b-yield relationships from other test sites adjusted to the North Korean site. However, the yield-scaling slope must be determined by modeling one of the smaller events, and the other tests are too small to have broadband P waves with adequate signal quality to model. If the elastic modeling with flat free-surface using the MM explosion model for a granite source medium is taken at face value, the t^* is close to that for the NTS and Amchitka sites, and the m_b-yield scaling coefficient, b, is thus likely higher than the values of 0.7 to 0.75 for the Soviet test sites. Murphy (1977) estimated a slope of 0.85 and Lay (1985) estimated amplitude-yield scaling coefficients of 0.77 to 0.92 for Nevada Test Site (NTS). Using the m_{bNEIC} value for the 2017 event (6.3) to calibrate magnitude-yield relationships for yield-scaling slopes of 0.75 (Semipalatinsk; Murphy et al., 2013), 0.81 (NTS, Murphy et al., 2013) and 0.9 (classic value for a high t^* site) gives yield estimates for the other five North Korean tests based on their m_{bNEIC} values (Table S2). These range from 0.5 to 17.8 kt, with factors of 1.5 to 3 variation in estimates for different slopes. The low number of observations for the 2006 and 2009 events raises questions about how reliable their m_{bNEIC} values are relative to the larger events. This exercise is specific to the USGS-NEIC magnitudes, and different intercept values must be calculated if the 2017 m_b estimate differs from 6.3 for a different catalog. Direct yield estimation for the smaller events will be presented in a forthcoming paper, resolving the yield scaling slope.

References

Avants, M. (2014). Effects of near-source heterogeneity on wave fields emanating from crustal sources observed at regional and teleseismic distances. (PhD thesis). (135 pp.). University of California, Santa Cruz.

Bache, T. C., Marshall, P. D., & Bache, L. B. (1985). Q for teleseismic P waves from central Asia. *Journal of Geophysical Research*, *90*(B5), 3575–3587. https://doi.org/10.1029/JB090iB05p03575

Burdick, L. J., & Helmberger, D. V. (1979). Time functions appropriate for nuclear explosions. *Bulletin of the Seismological Society of America*, *69*, 957–973.

Burdick, L. J., Wallace, T., & Lay, T. (1984). Modelling the near field and teleseismic observations from the Amchitka test site. *Journal of Geophysical Research*, *89*(B6), 4373–4388. https://doi.org/10.1029/JB089iB06p04373

Burger, R. W., Lay, T., & Burdick, L. J. (1987). Average *Q* and yield estimates from the Pahute Mesa test site. *Bulletin of the Seismological Society of America*, *77*, 1274–1294.

Denny, M. D., & Johnson, L. R. (1991). The explosion seismic source function: Models and scaling laws reviewed. In *Explosion source Phenomenology, Geophysical Monograph*, (Vol. 65, pp. 1–24). Washington DC: American Geophysical Union. https://doi.org/10.1029/GM065p0001

Der, Z., McElfresh, T., Wagner, R., & Burnetti, J. (1985). Spectral characteristics of *P* waves from nuclear explosions and yield estimation. *Bulletin of the Seismological Society of America*, *75*(2), 379–390.

Der, Z., Shumway, R. H., & Lees, A. C. (1987). Multichannel deconvolution of *P* waves at seismic arrays. *Bulletin of the Seismological Society of America*, *77*, 195–211.

Der, Z. A., Rivers, W. D., McElfresh, T. W., O'Donnell, A., Klouda, P. J., & Marshall, M. E. (1982). Worldwide variations in the attenuative properties of the upper mantle as determined from spectral studies of short-period body waves. *Physics of the Earth and Planetary Interiors*, *30*, 12–25.

Douglas, A., Marshall, P. D., & Young, J. B. (1987). The *P* waves from the Amchitka Island explosions. *Geophysical Journal of the Royal Astronomical Society*, *90*(1), 101–117. https://doi.org/10.1111/j.1365-246X.1987.tb00677.x

Futterman, W. I. (1962). Dispersive body waves. *Journal of Geophysical Research*, *67*(13), 5279–5291. https://doi.org/10.1029/JZ067i013p05279

Haskell, N. A. (1967). Analytic approximation for the elastic radiation from a contained underground explosion. *Journal of Geophysical Research*, *72*(10), 2583–2587. https://doi.org/10.1029/JZ072i010p02583

Helmberger, D. V., & Hadley, D. M. (1981). Seismic source functions and attenuation from local and teleseismic observations of the NTS events Jorum and Hadley. *Bulletin of the Seismological Society of America*, *71*, 51–67.

Hwang, Y. K., Ritsema, J., & Goes, S. (2011). Global variation of body-wave attenuation in the upper mantle from teleseismic P wave and S wave spectra. *Geophysical Research Letters*, *38*, L06308. https://doi.org/10.1029/2011GL046812

Ichinose, G., Woods, M., & Dwyer, J. (2014). Mantle attenuation estimated from regional and teleseismic *P*-waves of deep earthquakes and surface explosions. *Pure and Applied Geophysics*, *171*(3-5), 485–506. https://doi.org/10.1007/s00024-012-0632-z

Lay, T. (1985). Estimating explosion yield by analytical waveform comparison. *Geophysical Journal of the Royal Astronomical Society*, *82*(1), 1–30. https://doi.org/10.1111/j.1365-246X.1985.tb05126.x

Lay, T. (1991). The teleseismic manifestation of *pP*: Problems and paradoxes. In *Explosion source Phenomenology, Geophysical Monograph*, (Vol. 65, pp. 109–125). Washington DC: American Geophysical Union. https://doi.org/10.1029/GM065p0109

Lay, T., Helmberger, D. V., & Harkrider, D. G. (1984). Source models and yield-scaling relations for underground nuclear explosions at Amchitka Island. *Bulletin of the Seismological Society of America*, *74*, 843–862.

Minster, J. B. (1978). Transient and impulse responses of a one dimensional linearly attenuating medium. Part I. analytical results. *Geophysical Journal*, *52*(3), 479–501. https://doi.org/10.1111/j.1365-246X.1978.tb04245.x

Mueller, R. A., & Murphy, J. R. (1971). Seismic characteristics of underground nuclear detonations part I. Seismic spectrum scaling. *Bulletin of the Seismological Society of America*, *61*, 1675–1692.

Murphy, J. R. (1977). Seismic source functions and magnitude determinations for underground nuclear detonations. *Bulletin of the Seismological Society of America*, *67*, 135–158.

Murphy, J. R., Stevens, J. L., Kohl, B. C., & Bennett, T. J. (2013). Advanced seismic analyses of the source characteristics of the 2006 and 2009 North Korean nuclear tests. *Bulletin of the Seismological Society of America*, *103*(3), 1640–1661. https://doi.org/10.1785/0120120194

Ni, S., Helmberger, D., & Pitarka, A. (2010). Rapid source estimation from global calibrated paths. *Seismological Research Letters*, *81*(3), 498–504 . https://doi.org/10.1785/gssrl.81.3.498

Patton, H. J., & Pabian, F. V. (2014). Comment on "Advanced seismic analyses of the source characteristics of the 2006 and 2009 North Korean nuclear tests" by J. R. Murphy, J. L. Stevens, B. C. Kohl, and T. J. Bennett. *Bulletin of the Seismological Society of America*, *104*(4), 2104–2110. https://doi.org/10.1785/0120130262

Saikia, C. K. (2017). Time-domain source function (TDSF) for nuclear and chemical explosions—Analysis around Nevada National Security Site (NNSS). *Geophysical Journal International*, *209*(2), 1048–1063. https://doi.org/10.1093/gji/ggx072

Stevens, J. L., & Day, S. M. (1985). The physical basis of m_b: M_S and variable frequency magnitude methods for earthquake/explosion discrimination. *Journal of Geophysical Research*, *90*(B4), 3009–3020. https://doi.org/10.1029/JB090iB04p03009

von Seggern, D., & Blandford, R. (1972). Source time functions and spectra for underground nuclear explosions. *Geophysical Journal of the Royal Astronomical Society*, *31*(1-3), 83–97. https://doi.org/10.1111/j.1365-246X.1972.tb02360.x

Walter, W. R., & Priestley, K. F. (1991). High-frequency *P* wave spectra from explosions and earthquakes. In *Explosion Source Phenomenology, Geophysical Monograph*, (Vol. 65, pp. 219–228). Washington DC: American Geophysical Union. https://doi.org/10.1029/GM065p0219

Wang, T., Shi, Q., Nikkhoo, M., Wei, S., Barbot, S., Dreger, D., et al. (2018). The rise, collapse, and compaction of Mt. Mantap from the 3 September 2017 North Korean nuclear test. *Science*, eaar7230. https://doi.org/10.1126/science.aar7230